Adaptive mesh simulations of polycrystalline materials using a Cartesian representation of an amplitude expansion of the phase-field-crystal model

Matjaž Berčič* and Goran Kugler†
Department of Materials and Metallurgy, Faculty of Natural Sciences and Engineering, University of Ljubljana, Ljubljana, Slovenia

(Received 27 February 2018; published 11 September 2018)

This paper introduces improvements to an amplitude expansion of the phase-field-crystal model. An auxiliary field describing local grain rotation is introduced and used to enable the adaptive mesh to be coarsened in all grains, regardless of their orientation. Only a Cartesian representation of the amplitude equations is used.

DOI: 10.1103/PhysRevE.98.033303

I. INTRODUCTION

Many industrially important problems relate to the ability to understand and predict the microstructure evolution during thermomechanical processing of polycrystalline materials. In field of metallic materials, these include the processes of solidification, solid state phase transformations, recrystallization, grain growth, nucleation, and growth or dissolution of precipitates, etc. Predicting the microstructure's evolution generally requires accurate models to describe processes simultaneously occurring at various spatial and temporal scales, ranging from atomistic to mesoscopic and macroscopic and from atomic vibrations to diffusive times. Despite modern computational resources, even today these large variations in time and length scales in material modeling represent a huge research challenge. In past decades, several approaches were developed to study microstructure's evolution at various length scales, i.e., molecular dynamics and kinetic Monte Carlo on the atomistic scale, the cellular automata, Potts–Monte Carlo and phase-field (PF) methods on the mesoscopic scale, and continuum-based methods on the macroscopic scale [1]. To establish a way to bridge these models addressing phenomena at various scales, a range of approaches have been proposed [2,3]. In recent years, the materials engineering field has seen the increasingly popular concept of integrated computational materials engineering (ICME) which links material models at multiple scales hierarchically [4]. While approaches like ICME may be of great practical value by associating material models at different scales with processing technologies and product design, they may be associated with difficulties of discontinuous transitions between scales that can lead to nonphysical phenomena. In contrast, the PF method in combination with adaptive mesh refinement was used to study the microstructure evolution on spatial scales spanning several orders of magnitude [5,6]. Its success lies in expressing the boundary conditions on the solid-liquid interface with a partial differential equation for the evolution of a phase-field variable. As the evolved phase field is a continuous function of space, the method is not well suited for modeling phenomena occurring on an atomistic scale, as it is averaged out in the phase-field variable. To describe the atomic arrangement, the phase-field-crystal (PFC) methodology was introduced [7,8]. The PFC model is a reformulation of the Swift-Hohenberg model [9] and can be derived from classical density functional theory under some necessary assumptions [10]. The method uses a crystal density field to describe the dynamics of atomic structures. It incorporates elasticity and various topological defects in a natural way. Since the PFC method was initially developed, it has been improved in multiple ways, enabling it to be applied to even more problems. PFC models have been extended to describe materials with different crystal lattices using a two-mode PFC model [11], model structural transformations in materials using a constructed two-particle correlation function (XPFC model) [12,13], and extend this approach to stabilize several phases with a three-particle correlation function [14,15], incorporate acoustic waves [16] and spatial anisotropy [17], describe liquid crystals [18,19], and model phenomena occurring in ferromagnetic [20] and ferroelectric multicomponent materials [21].

One important PFC model improvement that is increasing in popularity is the complex-amplitude expansion (APFC) developed by Goldenfeld *et al.* [22,23]. The method uses a renormalization group based approach to express the atomic density function as a sum of waves, aligned with the reciprocal lattice vectors, and derives the evolution equations for the amplitudes. This approach offers the possibility to bridge the gap between the PFC method and PF methods. Such improvements greatly increase the size of the modeled material and, combined with other APFC method properties, offer the ability to study many phenomena in which larger volumes of material must be modeled at diffusive timescales. This extension has been successfully applied to the study of grain boundary motion and polycrystalline films [22–24], structural phase transitions [25], heteroepitaxial ordering of thin films [26–29], and grain boundary energies [30,31]. The method was initially developed for single-component systems with triangular symmetry in two dimensions (2D) and since then has been extended to binary systems [9,32,33], honeycomb [28,30] and square [25] lattices in 2D, and fcc and bcc systems [32,34] in three dimensions (3D). The APFC extension was also improved to obtain an instantaneous mechanical equilib-

*Corresponding author: matjaz.bercic@omm.ntf.uni-lj.si
†goran.kugler@omm.ntf.uni-lj.si

rium [35], tune the energy of defects and interfaces [31], and couple the microstructure forming fields to the hydrodynamic velocity field [36].

To further increase the size of the simulated domain, adaptive mesh refinement (AMR) algorithms can be applied to APFC models, as demonstrated by Athreya *et al.* [37]. Despite the AMR APFC model's initial success, some unresolved issues are preventing its further development [9]. Consequently, most of APFC models still use simple numerical methods on a fixed grid [9,24–30,32–36]. Therefore, the main purpose of this work is to propose a way for solving problems related to grain rotation in APFC models. The presented model does not require the use of separate phase and amplitude equations like in Athreya *et al.* [37]. Instead, an auxiliary local rotation field is calculated and used to align the basis vectors with the rotation of grains at all calculation points.

This contribution is organized as follows. In Sec. II, the main features of the PFC model and complex amplitude equations used in this work are recapitulated. Section III contains a description of the model, algorithm, and primary features of the numerical approach used. In Sec. IV, simulations results are presented and, finally, concluding remarks are given in Sec. V.

II. APFC MODEL

Evolution of the density field in the PFC model is given by [7]

$$\frac{\partial \rho}{\partial t} = \Gamma \nabla^2 \left(\frac{\delta \mathcal{F}}{\delta \rho} \right), \tag{1}$$

where $\mathcal{F}$ is the free energy functional dependent on local free energy density $f(\rho, \nabla^2 \rho)$ and Γ is a constant. The chosen free energy functional is minimized by a spatially uniform liquid state at high temperatures and by a spatially periodic "crystalline" phase at low temperatures [7]. A solution with the required form will naturally exhibit the properties observed in the crystals, such as the correct properties of elastic energy, defects in the crystalline phase, proper grain boundary energy, epitaxial growth, yield strength of nanocrystalline materials, and proper behavior of misfit dislocations as already shown by Elder *et al.* [7,8].

The exact form of the functional used is

$$f = \rho\left[\alpha \Delta T + \lambda\left(q_0^2 + \nabla^2\right)^2\right]\rho/2 + u\rho^4/4, \tag{2}$$

where α, λ, q_0, and u are model parameters that can be used to match the properties of a chosen material. The model's behavior can be better understood by first rewriting the free energy in dimensionless units using $\vec{x} = \vec{r} q_0$, $\psi = \rho\sqrt{u/\lambda q_0^4}$, $r = a\Delta T/\lambda q_0^4$, $\tau = \Gamma \lambda q_0^6 t$, and $F = \mathcal{F} u/\lambda^2 q_0^{8-d}$ into

$$F = \int d\vec{x}\{\psi[r + (1 + \nabla^2)^2]\psi/2 + \psi^4/4\}. \tag{3}$$

Conversion of the dynamic Eq. (1) yields

$$\frac{\partial \psi}{\partial t} = \nabla^2\{[r + (1 + \nabla^2)^2]\psi + \psi^3\}, \tag{4}$$

where $\varepsilon = u k_b T q_0^{d-4}/\lambda^2$. Equation (4) was introduced by Elder *et al.* [7,8] and since then has frequently been referred to as the PFC equation. The single mode solution of the PFC equation in the solid phase has triangular symmetry and can be approximated in terms of the complex amplitudes A_j [22,23,37] as

$$\psi \approx \sum_{j=1}^{3} A_j e^{i\mathbf{k_j}\cdot\mathbf{x}} + \sum_{j=1}^{3} A_j^* e^{-i\mathbf{k_j}\cdot\mathbf{x}} + \overline{\psi}, \tag{5}$$

where $\mathbf{k_j}$ are the reciprocal lattice vectors of a hexagonal crystal

$$\begin{aligned} \mathbf{k}_1 &= k_0(-\vec{i}\sqrt{3}/2 - \vec{j}/2), \quad \mathbf{k}_2 = k_0\vec{j}, \\ \mathbf{k}_3 &= k_0(\vec{i}\sqrt{3}/2 - \vec{j}/2), \end{aligned} \tag{6}$$

and k_0 the wave number set to $k_0 = 1$ in this work. This wave number corresponds to the atomic spacing of $a_0 = 2\pi/(\sqrt{3}/2)$. Dynamic equations for the coarse grained complex amplitudes have been derived by Goldenfeld *et al.* [22,23]:

$$\frac{\partial A_j}{\partial t} = \tilde{\mathcal{L}}_j A_j - 3A_j|A_j|^2 - 6A_j \sum_{k:k\neq j} |A_k|^2 - 6\overline{\psi} \prod_{k:k\neq j} A_k^*, \tag{7}$$

where $k, j \in [1, 3]$ and

$$\tilde{\mathcal{L}}_j = (1 - \nabla^2 - 2i\mathbf{k}_j \cdot \nabla)(-r - 3\overline{\psi}^2 - \{\nabla^2 + 2i\mathbf{k}_j \cdot \nabla\}^2) \tag{8}$$

is a rotationally covariant operator. The parameters $\overline{\psi}$ and r are the dimensionless average density and the dimensionless temperature proportional to the temperature difference to a critical temperature T_c. Due to rotational covariance of the operator $\tilde{\mathcal{L}}_j$, multiple orientations of the crystal grains can be modeled using only the set of basis vectors listed in (6).

Grain rotation in the complex-amplitudes equations (7) is represented by the so called beats in the amplitudes of grains, not aligned with the initial choice of basis vectors [22,37], as shown in Fig. 1. This makes adaptive mesh refinement techniques ineffective in solving the problem, as the mesh does not coarsen in misaligned grains due to the fast changing amplitudes caused by the beats. To tackle this problem, an improved approach using polar represen-

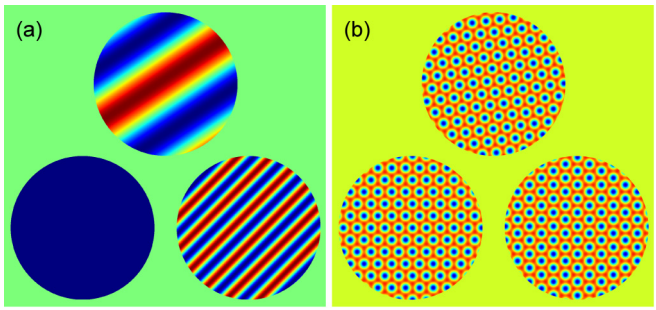

FIG. 1. Beats in misaligned grains. The images show (a) real component of the first complex amplitude $\mathrm{Re}(A_1)$, and (b) the reconstructed atomic density field ψ in three seeds, rotated for (clockwise from bottom left) $\theta = 0, \pi/24$, and $\pi/6$.

tation of the complex-amplitudes equations in combination with the existing representation was introduced by Athreya *et al.* [37]. The complex amplitudes were split into phase and amplitude as $A_j = \Psi_j e^{i\Phi_j}$ and both phase Φ and amplitude Ψ were evolved separately. The phase is computed as $\Phi = \arctan(\mathrm{Im}(A_j)/\mathrm{Re}(A_j))$ making phase Φ a locally discontinuous function, leading to calculation problems. To resolve problems with discontinuities, the simulation domain was divided into two subdomains: a liquid region, where the ordinary dynamic equations (7) were evolved, and a solidified region, where the phase and amplitude equations were used. Within the solidified region, an approximation of a frozen phase gradient was applied, which eliminated problems with the discontinuities of the phase gradient. As the conversion between representations is simple, the resulting computational scheme is efficient and produces significant speedups of the simulations originating from the added ability to coarsen the adaptive mesh within all grains, regardless of their orientation. The approximations used in the framework allow the efficient use of the computational resources, although some problems still remain. In particular, the problem of a hidden grain boundary between grains rotated by a multiple of the crystal's symmetry, as reported by Spatschek and Karma [9], is not easy to solve. Therefore, other approaches are needed to study the grain behavior under full grain rotation conditions. A possible approach is proposed in the following section.

III. DESCRIPTION OF THE MODEL

A. Local rotation of the basis vectors

The model exploits the fact that beats of complex amplitudes in solidified grains disappear, when the basis vectors for the amplitudes are correctly rotated. A local rotation field is introduced, and dynamic equations of the coarse grained complex amplitudes (7) are solved by taking into account the spatially dependent rotation of the basis vectors $\mathbf{k_j}$.

Density function of a grain rotated by ϑ with regard to the basis vectors can be written as [37]

$$\psi(\vartheta) = \sum_{j=1}^{3} A_j^{\vartheta} e^{i\mathbf{k}_j(\vartheta)\cdot\mathbf{x}} + \text{c.c.} + \overline{\psi}, \tag{9}$$

$$= \sum_{j=1}^{3} A_j^{\vartheta} e^{i\delta\mathbf{k_j}(\vartheta)} e^{i\mathbf{k}_j\cdot\mathbf{x}} + \text{c.c.} + \overline{\psi}, \tag{10}$$

$$= \sum_{j=1}^{3} A_j e^{i\mathbf{k}_j\cdot\mathbf{x}} + \text{c.c.} + \overline{\psi}, \tag{11}$$

where $\mathbf{k}_j(\vartheta) = \mathbf{k}_j + \delta\mathbf{k}_j(\vartheta)$ are rotated basis vectors and c.c. denotes the complex conjugate of the first sum. We derive the connection between the rotated amplitudes A_j^{ϑ} and nonrotated amplitudes A_j by comparing the terms associated with the same wave vectors and obtain

$$A_j = A_j^{\vartheta} e^{i\delta\mathbf{k}_j(\vartheta)\cdot\mathbf{x}}. \tag{12}$$

It follows that grains with arbitrary rotations can be described in terms of $\mathbf{k}_j$, with grain rotation resulting in beats of the amplitudes.

As the rotated amplitudes within a perfect, rotated grain remain constant, the gradient of the rotated amplitudes inside is zero:

$$\nabla A_j^{\vartheta} = (\nabla A_j) e^{-i\delta\mathbf{k}_j\cdot\mathbf{x}} + A_j(-i\delta\mathbf{k}_j) e^{-i\delta\mathbf{k}_j\cdot\mathbf{x}} = 0. \tag{13}$$

From (13) it follows that for a local rotation, at which beats disappear, the following must hold for the rotated basis vectors:

$$\delta\mathbf{k}_j(\vartheta) = \frac{\nabla A_j}{i A_j} = \mathbf{k}_j(\vartheta) - \mathbf{k}_j. \tag{14}$$

In simulations we know the amplitudes A_j, but not the local grain rotation. From (14) we can derive the local rotation of the grain in which the beats disappear.

Due to rotational covariance of the operator $\tilde{\mathcal{L}}_j$ and all of its parts used in the calculation, it follows that conversion between basis vectors rotated by a different amount can be separated from the operator evaluation. The operator defined as

$$\Box^{\vartheta} = [\nabla^2 + 2i\mathbf{k}_j(\vartheta)\cdot\nabla] \tag{15}$$

is rotationally covariant and therefore the following must hold:

$$\Box^{\vartheta} A_j^{\vartheta} = e^{-i\delta\mathbf{k}\cdot\mathbf{x}} \Box A_j, \tag{16}$$

where $\Box = \Box^{\vartheta=0}$. Further, if we separate operator $\tilde{\mathcal{L}}_j$ into two operators that can each be evaluated in a single step with a simple differential schema

$$\tilde{\mathcal{L}}_{1j}^{\vartheta} = (-r - 3\overline{\psi}^2 - (\Box^{\vartheta})^2), \tag{17}$$

$$\tilde{\mathcal{L}}_{2j}^{\vartheta} = (1 - \Box^{\vartheta}), \tag{18}$$

$$\tilde{\mathcal{L}}_j^{\vartheta} = \tilde{\mathcal{L}}_{2j}^{\vartheta} \tilde{\mathcal{L}}_{1j}^{\vartheta}, \tag{19}$$

then both $\tilde{\mathcal{L}}_{1j}$ and $\tilde{\mathcal{L}}_{2j}$ are rotationally covariant. This allows us to apply dynamic evolution equation even when the rotation of the basis vectors is spatially dependent.

We can numerically apply an operator $\tilde{\mathcal{O}}^{\vartheta}$ to a locally rotated field X:

$$\tilde{\mathcal{O}}^{\vartheta(\mathbf{x})}\, X^{\vartheta(\mathbf{x})}(\mathbf{x}) = \sum_{\tilde{\mathbf{x}}} \Gamma_{\tilde{\mathbf{x}}} e^{-i[\mathbf{k}(\mathbf{x})-\mathbf{k}(\tilde{\mathbf{x}})]\cdot\tilde{\mathbf{x}}} X^{\vartheta(\tilde{\mathbf{x}})}(\tilde{\mathbf{x}}), \tag{20}$$

where the summation goes over all neighbors included in the operator's evaluation. $\tilde{\mathcal{O}}$ can be any of the rotationally covariant operators $[\tilde{\mathcal{O}} \in \{\tilde{\mathcal{L}}_j^{\vartheta}, \tilde{\mathcal{L}}_{1j}^{\vartheta}, \tilde{\mathcal{L}}_{2j}^{\vartheta}\}]$ applied to any of the derived fields $[X \in \{A_j^{\vartheta}, \tilde{\mathcal{L}}_{1j} A_j^{\vartheta}, \tilde{\mathcal{L}}_j A_j^{\vartheta}\}]$. $\tilde{\mathbf{x}}$ is the location of the neighbor matching the operator kernel element $\Gamma_{\tilde{\mathbf{x}}}$. To convert between local rotations at $\mathbf{x}$ and $\tilde{\mathbf{x}}$, we need to multiply $X^{\vartheta(\tilde{\mathbf{x}})}(\tilde{\mathbf{x}})$ with a rotation conversion factor $e^{-i[\mathbf{k}(\mathbf{x})-\mathbf{k}(\tilde{\mathbf{x}})]\cdot\tilde{\mathbf{x}}}$, which needs to be stored alongside the values of $X^{\vartheta(\mathbf{x})}(\mathbf{x})$.

B. Algorithm description

When considering the evolution of the complex amplitudes in a system where the basis vectors for the amplitudes vary with location, one must take into account differences in rotation when applying the dynamic equations. Since all the fields needed in intermediate steps of the calculation are rotationally

Algorithm 1 Top level algorithm for evolution of complex amplitudes.

loop
  if $step\%adaptation = 0$ **then**
    Do mesh refinement
    Calculate local rotation
    Calculate rotation conversion factors
  end if
    Perform evolution iteration
end loop

covariant, this does not pose a problem apart from an additional multiplication step and the necessity of maintaining the rotational constants stored in the computational nodes. The calculation works in the same way as if all neighbor nodes of the current calculation node were temporarily converted in the same rotated system as the central node. When all basis vectors are the same, the normal evolution Eq. (7) can be applied.

Averaging over nodes, either when calculating ghost node values or when calculating values on the newly created nodes during mesh adaptation is carried out using Eq. (20). As changes in a local rotation affect the averaging of the fields, a small change in a local rotation is an additional criterion for mesh coarsening. The mesh adaptation algorithm therefore coarsens the mesh only where the change in a local rotation and all fields is sufficiently small.

The local rotation is calculated from the gradient of the complex amplitudes, and gradients change rapidly on the solid-liquid interface and in the vicinity of dislocations. To prevent large changes in a local rotation, which could result in skipped beats, an additional averaging step to remove high frequency changes is performed before the rotation angle update. The pseudocode of the implementation is shown in Algorithms 1 and 2.

Since our model employs local orientations of the basis vectors, and the original model is rotationally covariant, the properties of both models are equivalent under the assumptions of the complex-amplitudes model given with Eq. (7). An explicit iteration scheme was used in the implementation. Each complex amplitude is evolved using Eq. (7) on an adaptive grid. In all the calculations presented in this work, the parameters were set to match those used by Athreya in [37]; i.e., $r = -0.25$, $\overline{\psi} = 0.285$ with time step set to $\Delta t = 0.04$ and minimal grid spacing $\delta x_{\min} = \pi/2$. In grid adaptation, the change of amplitudes over one node is limited by $|A_j^{\vartheta,\ulcorner} - A_j^{\vartheta,\urcorner}| + |A_j^{\vartheta,\urcorner} - A_j^{\vartheta,\lrcorner}| + |A_j^{\vartheta,\lrcorner} - A_j^{\vartheta,\llcorner}| + |A_j^{\vartheta,\llcorner} - A_j^{\vartheta,\ulcorner}| <$ adapt threshold $= 0.02$ for each j, where the notation $^{\ulcorner}$ in $A_j^{\vartheta,\ulcorner}$ denotes the top left neighbor of the node. The maximal change is further limited by an additional criterion that the maximal change in a local rotation over one node must not exceed $\max_{\Delta\vartheta} = \pi/16$.

An AMR Solver was used in all the simulations, based on the work of Greenwood. The solver's implementation is described in [37–39].

Algorithm 2 Local rotation adjustment. Parameters p, q, $B_{\text{min amp}}$, and $\vartheta_{\text{max phase}}$ are heuristic.

for each computation node **do**
  Find optimal rotation ϑ_{opt}:
  if $|A_j^{\vartheta}| > A_{\text{min amp}}$ **then**
    In solidified regions: from gradient
    for all $j \in \{1, 2, 3\}$ **do**
      $\delta\mathbf{k}_j(\vartheta_{\text{current}}) = \text{Re}\left(\frac{\nabla A_j^{\vartheta_{\text{current}}}}{iA_j^{\vartheta_{\text{current}}}}\right)$
      $\vartheta_{x,j} = 1 + \mathbf{k}_j(\vartheta_{\text{current}}) \cdot \delta\mathbf{k}_j$
      $\vartheta_{y,j} = [\mathbf{k}_j(\vartheta_{\text{current}}) \times \delta\mathbf{k}_j] \cdot \hat{\mathbf{e}}_z$
    end for
    $\vartheta_{\text{opt}} = \vartheta_{\text{current}} + \text{atan2}\left(\sum_j \vartheta_{y,j}/3, \sum_j \vartheta_{x,j}/3\right)$
  else
    In liquid regions: drop towards zero
    $\vartheta_{\text{opt}} = 0$
  end if
  Smooth the changes
  $\vartheta_{\text{new}} = p \times \vartheta_{\text{current}} + q \times \vartheta_{\text{opt}}$
  Prevent skipping beats
  $d\vartheta = \max_{\{\text{all neighbors NN}\}} |\vartheta_{\text{NN}} - \vartheta_{\text{new}}|\text{modulo } 2\pi$
  $k_\vartheta = dx\, d\vartheta/\vartheta_{\text{max phase}}$
  if $k_\vartheta > 1$ **then**
    $\vartheta_{\text{new}} = \vartheta_{\text{current}} + (\vartheta_{\text{new}} - \vartheta_{\text{current}})/k_\vartheta$
  end if
  $\vartheta_{\text{current}} = \vartheta_{\text{new}}$
end for

IV. RESULTS

Figure 2 shows evolution of the microstructure represented by the average amplitude field ($\sum_j |A_j|/3$), of an example problem in which 12 seeds with an initial radius of 8π and orientation angles in the range $[0, \pi/12)$ were placed inside a square domain of size 256π with a periodic boundary condition. The example problem was chosen to match the example configuration employed by Athreya *et al.* in [37] as closely as possible to allow the reader to make an easy comparison. Note that the grain rotations are different and thus the number of dislocations on different grain boundaries is not the same as in [37]. A visible example is the grain boundary on the bottom right part of the simulation domain where in our simulations dislocations do not appear due to a small difference in the rotations of the impinging grains.

By introducing a local rotation field in combination with exploitation of the rotational covariance of all steps in the calculation, we were able to solve the complex-amplitudes equations on an adaptive grid, with coarsening in all grains, regardless of their orientation. This ensures the computational resources spent on calculations scale with the grain surface in the same manner as achieved by Athreya *et al.* [37]. In comparison, our approach does not require different representations of the complex amplitudes in different regions of the computational domain, which eliminates difficulties that could arise from application of two different evolution equations in separate regions of the simulation domain. However, compared to the basic APFC model described by Goldenfeld *et al.* [22,23], this model requires additional multiplications and memory for the storage and application of the rotation factors.

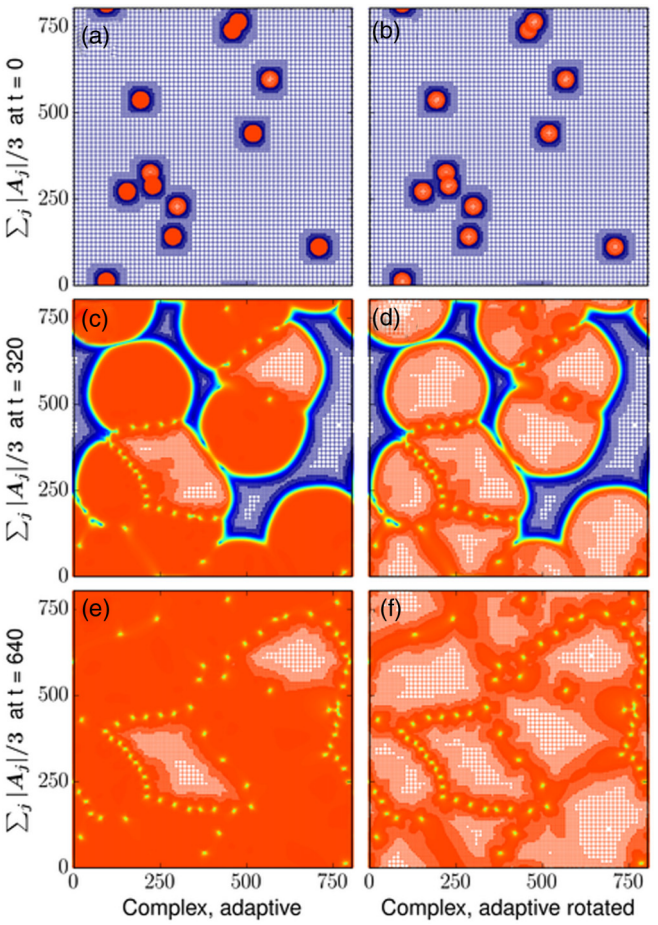

FIG. 2. Microstructure evolution in time. Comparison of the AMR model with and without local rotation. When using a local rotation, the mesh coarsens in all seeds, regardless of their orientation, and remains dense on grain boundaries where dislocations are formed. Images show the average amplitude field ($\sum_j |A_j|/3$) at different times.

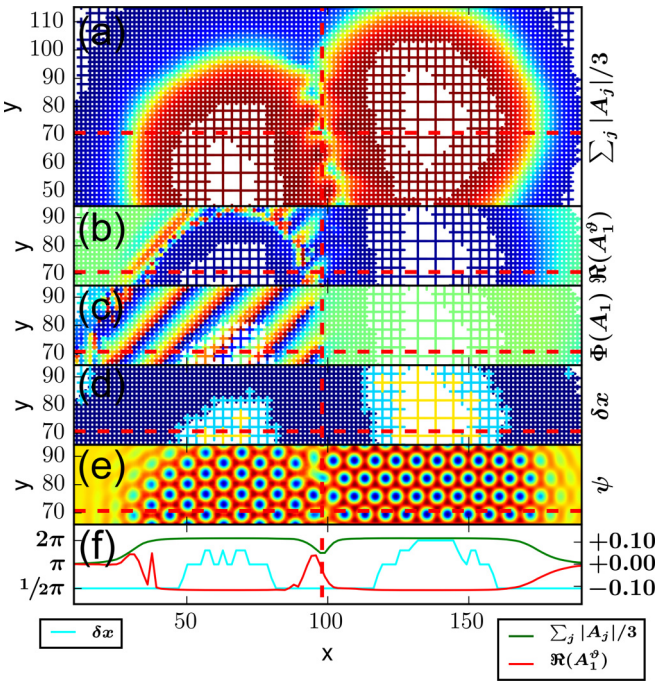

FIG. 3. Beats and mesh refinement in rotated and nonrotated grains. The grains are rotated by $\theta = \pi/12$ and 0. From top to bottom the image shows (a) the average absolute amplitude ($\sum_j |A_j|/3$), (b) the real part of locally rotated complex amplitude [$\mathrm{Re}(A_1^\vartheta)$], (c) the phase angle of the complex amplitude A_1 [$\Phi(A_1)$], (d) local mesh refinement (δx), (e) reconstructed atomic density function (ψ), and (f) the fields δx, $\sum_j |A_j|/3$ in cross section.

The evolution of the microstructure shown in Fig. 2 shows the results obtained with our algorithm closely match the results obtained with the previous approach. The positions of the dislocations and the resulting microstructure overall are the same, while the grid remains dense only on the solid-liquid interface and around the dislocations, where the field values change more rapidly.

A better insight into our model's properties can be obtained by analyzing the results displayed in Fig. 3 where the impingement of two grains was simulated. The left grain is rotated by $\pi/12$ and therefore exhibits the amplitude beats in all amplitudes, whereas the right grain is aligned with the choice of basis vectors and shows no beats. This may be seen in the Fig. 3(c) on the third row where the phase of the first complex amplitude $\Phi(A_1)$ is shown, indicating beats in the left grain and no beats in the right grain. The introduced locally rotated complex amplitude A_1^ϑ is shown on the second row in Fig. 3(b), where we can see that no beats are exhibited in the interior of either grain, where our algorithm is able to align the orientation of the basis vectors with the rotated grain on the left and remove all the beats. It can be observed that when using a local rotation, the mesh coarsens inside both grains, regardless of their orientation, and remains dense on the boundary between the grains.

In order to more clearly demonstrate how our model behaves, we simulated the growth of 12 grains placed in an undercooled melt in different locations. As may be seen in Fig. 4, the results obtained using our model are in excellent agreement with the results obtained without local rotation and with results obtained on a regular grid. The comparison shows that our model successfully reproduces the microstructure with grid coarsening in all grains. Figure 4 shows a snapshot of the microstructure's evolution at $t = 360$. Results obtained with different models are placed in consecutive columns of Fig. 4: the first column shows the APFC model on a uniform grid, the second column the APFC model on an adaptive grid, while the third column shows our model. Images in the rows display the following fields: (a)–(c) reconstructed atomic density field ψ, (d)–(f) mesh density δx, (g)–(i) average amplitude $\sum_j |A_j|/3$, (j)–(l) real part of the first complex amplitude $\mathrm{Re}(A_1)$, and (m)–(o) local grain rotation θ in degrees. The reconstructed atomic density field ψ shown in the first row (a)–(c) is virtually the same in all models used. In the images showing mesh density δx in the second row (d)–(f) we can see that when applying AMR techniques to the APFC model, the mesh coarsens only in liquid regions and nonrotated grains, whereas when using our approach the mesh coarsens in all grains, and dense mesh remains only around the dislocations and at the solid-liquid interface.

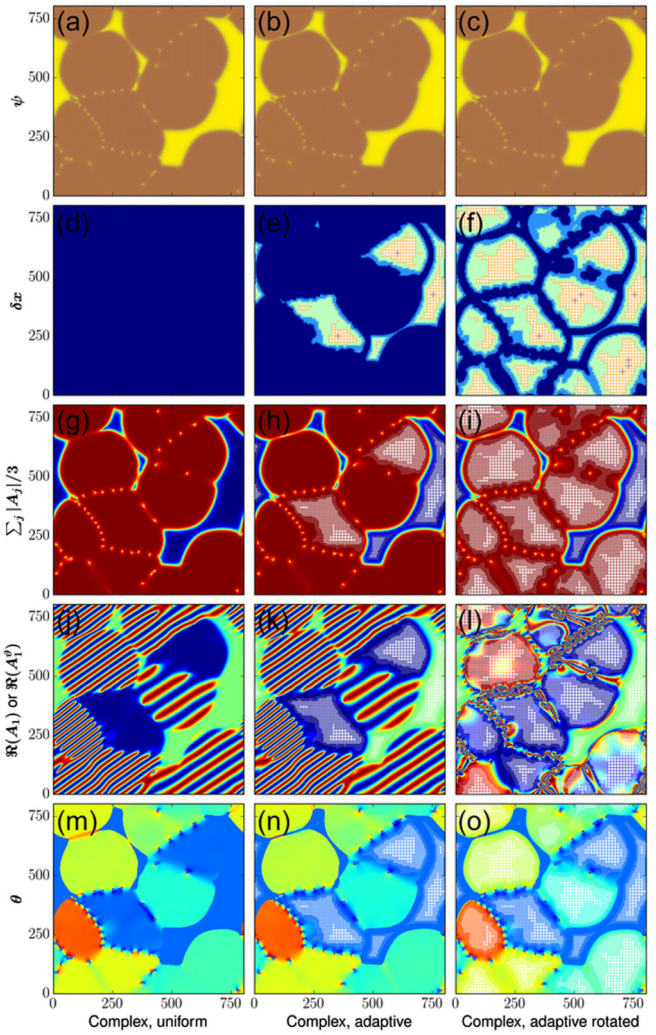

FIG. 4. Comparison of simulation results with different models at $t = 360$. All columns show PFC model with complex-amplitudes extension. The first column shows results when using a regular grid, the second column shows results when using adaptive mesh refinement techniques, and the third column shows results when using local rotation with the help of an auxiliary rotation field. From top to bottom: reconstructed atomic density field ψ, mesh density δx, average amplitude $\sum_j |A_j|/3$, real part of the first complex amplitude $\mathrm{Re}(A_1)$, and local grain rotation in degrees θ are shown.

Average amplitude $\sum_j |A_j|/3$ presented in the third row (g)–(i) shows the same grain growth and locations of dislocations are obtained with all three models. The fourth row presents the real component of the first complex amplitude $\mathrm{Re}(A_1)$ in the columns corresponding to APFC models without a local rotation (j)–(k). We can observe the beats occurring in rotated grains that prevent the mesh from coarsening. As our model uses a locally rotated complex amplitude field A_j^{ϑ} instead of A_j, the real part of this field is shown in the last column (l). We can see that the local rotation eliminates beats in all grains and enables efficient mesh coarsening. The last row shows local grain rotation. Images corresponding to APFC models (m) and (n) show a local rotation field obtained in post-processing, which is not used during calculations and is displayed here only for comparison. The final image in the last row (o) shows

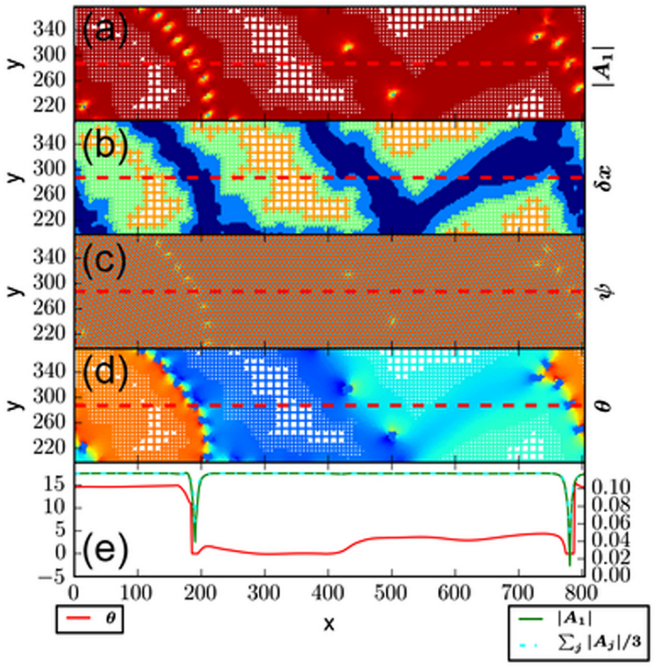

FIG. 5. Selected variables in excerpt and cross section at $t = 560$. From top to bottom: (a) absolute value of the first complex amplitude $|A_1|$, (b) local mesh refinement δx, (c) reconstructed density field ψ, and (d) local rotation θ. Values of θ, $|A_1|$, and $\sum_j |A_j|/3$ in cross section on the marked line at $y = 183\pi/2 \approx 287$ are shown in the last image (e). The local rotation field correctly tracks the grain rotation and shows large changes only on the grain boundaries.

the local rotation field θ as used during the calculations in our model. We can observe that the density of dislocations on the boundary between grains corresponds to the difference in the rotation of the grains. When rotations of two grains differ only slightly, no dislocations form on the boundary. In the bottom left part of the simulation domain, we placed two seeds with the same orientation, but shifted the lattice of one seed by approximately half of the lattice spacing with regard to the second seed. On the boundary between these two grains we can therefore find no dislocations since the orientation is the same. However, because the atomic lattice is shifted in one grain with regard to the other, the mesh still does not coarsen completely as some elastic deformations remain in the atomic lattice and variations in amplitudes due to the elastic deformations requiring higher mesh refinement. We can also observe that shifting the atomic lattice changes the phase of both locally rotated amplitudes A_j^{ϑ} and A_j. As the phase changes continuously, no defects appear on this boundary.

Selected fields in the cross section of the same simulation are shown in Fig. 5, where the changes in local rotation field θ across the grain boundaries can be better tracked. Rapid changes can be observed where the cross-section cut approaches the dislocation ($x \approx 200$) and the local rotation rapidly switches between rotations of both interfacing grains. A more gradual change in local rotation is observed on the interfaces between grains which differ in rotation by a smaller amount ($x \approx 480$ and $x \approx 650$), where the cut line does not pass directly through a dislocation. We can see that the

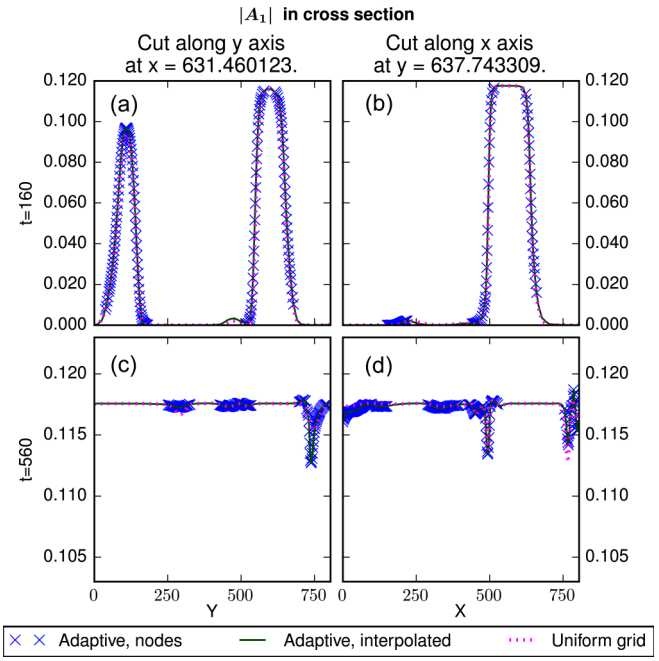

FIG. 6. Amplitude $|A_1|$ in cross section cut along the lines $x = 201\pi \approx 631$ and $y = 203\pi \approx 638$ at times $t = 160$ and 560. Results obtained with AMR using a local rotation on an adaptive grid match the results obtained with simulations on a uniform grid. Exact values at the intersected computation nodes of the adaptive grid are shown in combination with interpolated values from the same grid in comparison with values obtained on a uniform grid.

mesh is refined only on the grain boundaries and remains refined even on the boundary between grains which vary only slightly in their orientations and dislocations do not appear ($x \approx 650$). This is needed due to the elastic deformations that appear there to accommodate the deformation of the crystal lattice.

A comparison with the results obtained on a regular grid is shown in Fig. 6 where the field $|A_1|$ is shown in cross section. The results are compared at two different times, in the top row (a) and (b) at $t = 160$ where the seeds are still growing into the undercooled melt, and in the bottom row (c) and (d) at $t = 560$ when the entire simulation domain has already solidified. The comparison is made between the exact values obtained on the computational nodes of the adaptive mesh that lie exactly on the cross-section cut line, interpolated values from the adaptive mesh and results obtained on the uniform grid. All results are in excellent agreement, with small differences observed only at the solid-liquid interface and grain boundaries.

As expected, the number of computational nodes required in our approach is similar to that achieved by Athreya *et al.* [37] using a hybrid implementation. During simulation of the solidification, the number of computational nodes grows linearly in time at first, as the interface of the growing grains becomes larger, which may be seen in Fig. 7. As the mesh coarsening can be achieved in all grains, regardless of their orientation, the final number of computational nodes is significantly lower than the number of nodes of a regularly spaced grid of a similar size.

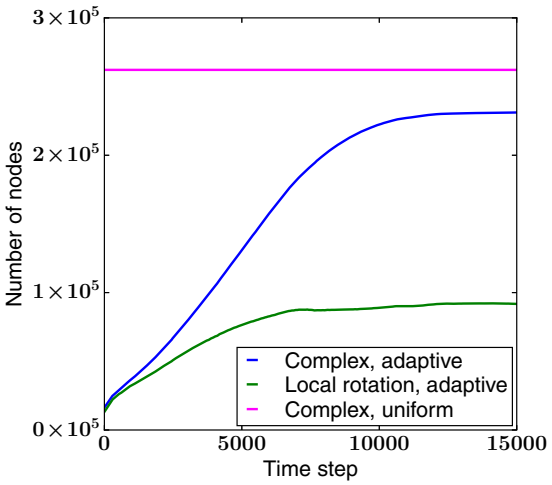

FIG. 7. Number of computational nodes as a function of time for the summations shown in Figs. 2 and 4. After the liquid freezes, the number of nodes stops increasing. When using the scheme with a local rotation, the mesh coarsens in all nodes and therefore consists of a much smaller total number of nodes.

In order to further verify that the introduction of a local rotation field does not introduce additional errors into the calculation when local rotation is not correctly determined, we ran two simulations of an example with three seeds in an undercooled melt, shown in Fig. 8. One of the seeds was rotated by 2.5°, and the other two by 7.5°. The atomic lattices of two seeds with the same rotation were mutually shifted by half of the lattice spacing, resulting in an area with pure elastic deformation without rotation (at $x \approx 280$ in Fig. 8). In the first simulation run we let our algorithm determine the best local rotation field, and in the second run we set the local rotation field to a chosen, time independent function $\Theta(\mathbf{x}) = \Theta(x)$. We chose to use a regular grid for this simulation, as this eliminates numerical errors originating from AMR and allows for a better understanding of errors originating from imprecisions in determining the local rotation. The simulations shown in Fig. 8 show that the microstructure obtained in both simulation runs is virtually the same, with minor differences only around dislocation cores. The first row of the image (a) shows the microstructure obtained when our algorithm determines the local rotation and the second row (b) shows the case where we fix the local rotation to a time independent function $\Theta(x)$. The third row (c) shows local rotation as determined by our algorithm. Possible performance of our algorithm is limited by the amount of deformation that remains in the rotated amplitudes A_j^{ϑ} after rotation and this remainder $\Delta\epsilon = \sqrt{\sum_{i,j} E_{i,j}}$ is presented in the fourth row image (d) and in cross section in the bottom row (e) in Fig. 8. Local rotation Θ as determined by our algorithm and the imposed rotation $\Theta(x)$ used in our second simulation run is shown in cross-section plots in the last row image (e) as well. $\mathbf{E}$ is defined as

$$\mathbf{E} = \mathbf{R}(-\vartheta)\mathbf{F} - \mathbf{I}, \tag{21}$$

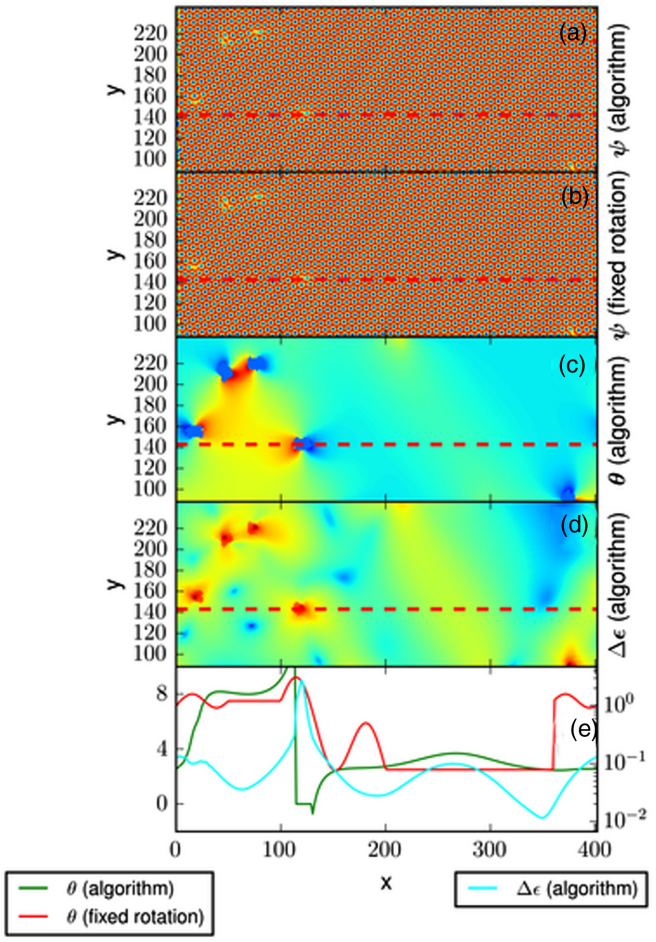

FIG. 8. Accuracy of the simulations under conditions where local rotation might be incorrectly calculated or where large deformations exist. (a) Microstructure of a simulation run where our algorithm determined local rotation. (b) Microstructure of a simulation run where local rotation was fixed to a chosen function $\Theta(\mathbf{x}) = \Theta(x)$. The microstructure in both simulation runs matches closely, with minor differences observed only around dislocations. (c) Local rotation field Θ as determined by our algorithm. (d) Deformation remainder $\Delta\epsilon$, shown in logarithmic scale. (e) Local rotation Θ as determined by our algorithm, the chosen function $\Theta(x)$, and deformation remainder $\Delta\epsilon$ in cross section. $\Delta\epsilon$ remains low inside grains, in the area with pure elastic deformation at $x \approx 280$ shows a small increase coupled with some inaccuracy in the calculation of a local rotation field Θ and rapidly increases in the vicinity of the dislocation at $x \approx 120$.

where ϑ is the rotation determined by our algorithm and $\mathbf{F}$ is the deformation gradient [35], defined as

$$\mathbf{F} = \mathbf{I} + \nabla\mathbf{u} = \mathbf{I} + \frac{2}{3}\sum_{j=1}^{3}\mathbf{k}_j \nabla[\arg(A_j)]. \tag{22}$$

As the deformation gradient can be split into rotation $\mathbf{R}(\tilde{\vartheta})$ and pure deformation $\mathbf{U}$ by polar decomposition as $\mathbf{F} = \mathbf{R}(\tilde{\vartheta})\mathbf{U}$, the parameter $\Delta\epsilon$ vanishes when our algorithm can determine the correct local rotation ($\vartheta = \tilde{\vartheta}$) and there is no pure deformation ($\mathbf{U} = \mathbf{I}$). In the last row in Fig. 8 we can see that the local rotation removes almost the entire deformation in the interior of grains with $\Delta\epsilon$ quickly dropping below 0.05. Around dislocations and on the grain boundaries, a significant portion of the deformation remains, but this does not result in increased errors in the calculations. The comparison between images in the first and second rows in Fig. 8 shows that the microstructure remains the same even if we use incorrect local rotation in large areas of the computational domain. This is a consequence of rotational covariance of evolution equations, and due to this property the calculations are independent of the actual rotation used. Additional errors are not introduced due to possible inaccuracies in the calculation of a local rotation field. Our method is best understood as an exploit of the rotational covariance of the evolution equations that locally transform the equations to a set of rotated amplitudes A_j^{ϑ}, defined on a set of basis vectors aligned with the local grain. This removes fast variations of the real and imaginary parts of the complex amplitudes in misaligned grains that originate from rotation of the grain. With only slow variations in complex amplitudes remaining, the AMR can be effectively used in the entire simulation domain using only the Cartesian representation.

Therefore, the idea of a local rotation should not be understood as a way to approximate values of the complex amplitudes and does not require additional assumptions to work. Just as AMR can be applied to a basic complex-amplitudes model, our model can be used in cases where large deformations are expected. When rotated grains are simulated with basic complex-amplitudes models, the use of AMR is ineffective as the high spatial variations of amplitudes require high mesh refinement, but does not produce inaccurate results. The computational mesh refines and computational efficiency is lost, but not the accuracy. When areas with large deformations are encountered in our model, the local rotation cannot eliminate the variations in the Cartesian representation of the complex amplitudes and the mesh refines. This results in the same accuracy as we would achieve without local rotation, with some loss in the computation speed.

Aside from enabling the coarsening of the computational mesh in all grains using only the Cartesian representation of the amplitude equations, our model helps to resolve another pressing issue of modeling with complex-amplitude equations. With some additional improvements, to be reported in detail elsewhere, we were able to eliminate an unphysical grain boundary that appears when the misfit between the impinging grains approaches the crystal's symmetry rotation (60° in our case). As reported by Spatschek and Karma [9], the amplitude equations' formalism is unable to properly model grain boundaries where interfacing grain rotations differ by more than half of the angle of the crystal symmetry rotation. Our initial simulations indicate that improvements resulting in the use of a local rotation field could also lead to better modeling of grain boundaries for a whole range of misorientations.

V. CONCLUSIONS

A model is presented for solving complex-amplitude equations on an adaptive mesh, which solves the problem of beats in misaligned grains and allows for mesh coarsening in all grains. It is based on the observation that the beats disappear when the basis vectors for the amplitudes are correctly rotated.

The proper rotation of the basis vectors was derived from the complex amplitudes and stored in an auxiliary variable used in calculations. The rotational covariance of the operators used in the evolution of the complex amplitudes allowed us to separate the conversion between differently rotated fields from the evolution equations. The results obtained using our approach closely match the results obtained with existing models.

Our model's computational efficiency scales in the same way as the hybrid approach described by Athreya *et al.* in [37]. The model does not require a presumption of a frozen phase gradient inside the solidified grains and uses only the Cartesian representation of the fields in the entire computational domain. The model shows promise with regard to modeling grains of a larger rotation range. With some improvements to the model, the unphysical grain boundary between grains which differ in rotation by a multiple of the crystal's symmetry rotation can be removed.

We confirmed that the model is resilient to inaccuracies in the calculation of a local rotation angle, and does not introduce errors into calculations even in areas where large strains exist. This is an expected consequence of the main idea of our model: it is an exploit of the rotational covariance of the evolution equations, aimed at enabling AMR mesh coarsening in all grains.

ACKNOWLEDGMENTS

We thank M. Greenwood for sharing his implementation of the AMR solver described in [38,39], from which we developed our code. The authors acknowledge financial support from the Slovenian Research Agency (research core funding Grants No. 1000-17-0510 and No. P2-0344), and would like to thank the Slovenian Initiative for the National Grid (SLING) for the computational resources on the Arnes cluster.

[1] D. Raabe, *Computational Materials Science* (Wiley-VCH, Weinheim, 1998).
[2] E. Weinan, *Principles of Multiscale Modeling* (Cambridge University Press, Cambridge, 2011).
[3] K. Matouš, M. G. Geers, V. G. Kouznetsova, and A. Gillman, J. Comput. Phys. **330**, 192 (2017).
[4] M. F. Horstemeyer, *Integrated Computational Materials Engineering (ICME) for Metals* (Wiley, Hoboken, NJ, 2012).
[5] N. Provatas and K. Elder, *Phase-Field Methods in Materials Science and Engineering* (Wiley, Hoboken, NJ, 2010).
[6] N. Provatas, N. Goldenfeld, and J. Dantzig, Phys. Rev. Lett. **80**, 3308 (1998).
[7] K. R. Elder, M. Katakowski, M. Haataja, and M. Grant, Phys. Rev. Lett. **88**, 245701 (2002).
[8] K. R. Elder and M. Grant, Phys. Rev. E **70**, 051605 (2004).
[9] R. Spatschek and A. Karma, Phys. Rev. B **81**, 214201 (2010).
[10] K. R. Elder, N. Provatas, J. Berry, P. Stefanovic, and M. Grant, Phys. Rev. B **75**, 064107 (2007).
[11] K.-A. Wu, A. Adland, and A. Karma, Phys. Rev. E **81**, 061601 (2010).
[12] M. Greenwood, N. Provatas, and J. Rottler, Phys. Rev. Lett. **105**, 045702 (2010).
[13] M. Greenwood, N. Ofori-Opoku, J. Rottler, and N. Provatas, Phys. Rev. B **84**, 064104 (2011).
[14] G. Kocher and N. Provatas, Phys. Rev. Lett. **114**, 155501 (2015).
[15] M. Seymour and N. Provatas, Phys. Rev. B **93**, 035447 (2016).
[16] P. Stefanovic, M. Haataja, and N. Provatas, Phys. Rev. Lett. **96**, 225504 (2006).
[17] R. Prieler, J. Hubert, D. Li, B. Verleye, R. Haberkern, and H. Emmerich, J. Phys.: Condens. Matter **21**, 464110 (2009).
[18] R. Wittkowski, H. Löwen, and H. R. Brand, Phys. Rev. E **82**, 031708 (2010).
[19] R. Wittkowski, H. Löwen, and H. R. Brand, Phys. Rev. E **83**, 061706 (2011).
[20] N. Faghihi, N. Provatas, K. R. Elder, M. Grant, and M. Karttunen, Phys. Rev. E **88**, 032407 (2013).
[21] M. Seymour, F. Sanches, K. Elder, and N. Provatas, Phys. Rev. B **92**, 184109 (2015).
[22] N. Goldenfeld, B. P. Athreya, and J. A. Dantzig, Phys. Rev. E **72**, 020601 (2005).
[23] N. Goldenfeld, B. P. Athreya, and J. A. Dantzig, J. Stat. Phys. **125**, 1015 (2006).
[24] B. P. Athreya, N. Goldenfeld, and J. A. Dantzig, Phys. Rev. E **74**, 011601 (2006).
[25] N. Ofori-Opoku, J. Stolle, Z.-F. Huang, and N. Provatas, Phys. Rev. B **88**, 104106 (2013).
[26] K. R. Elder, G. Rossi, P. Kanerva, F. Sanches, S.-C. Ying, E. Granato, C. V. Achim, and T. Ala-Nissila, Phys. Rev. Lett. **108**, 226102 (2012).
[27] K. R. Elder, G. Rossi, P. Kanerva, F. Sanches, S.-C. Ying, E. Granato, C. V. Achim, and T. Ala-Nissila, Phys. Rev. B **88**, 075423 (2013).
[28] K. R. Elder, Z. Chen, K. Elder, P. Hirvonen, S. Mkhonta, S.-C. Ying, E. Granato, Z.-F. Huang, and T. Ala-Nissila, J. Chem. Phys. **144**, 174703 (2016).
[29] M. Smirman, D. Taha, A. K. Singh, Z.-F. Huang, and K. R. Elder, Phys. Rev. B **95**, 085407 (2017).
[30] P. Hirvonen, M. M. Ervasti, Z. Fan, M. Jalalvand, M. Seymour, S. M. Vaez Allaei, N. Provatas, A. Harju, K. R. Elder, and T. Ala-Nissila, Phys. Rev. B **94**, 035414 (2016).
[31] M. Salvalaglio, R. Backofen, A. Voigt, and K. R. Elder, Phys. Rev. E **96**, 023301 (2017).
[32] K. R. Elder, Z.-F. Huang, and N. Provatas, Phys. Rev. E **81**, 011602 (2010).
[33] Z.-F. Huang, K. R. Elder, and N. Provatas, Phys. Rev. E **82**, 021605 (2010).
[34] K. R. Elder and Z.-F. Huang, J. Phys.: Condens. Matter **22**, 364103 (2010).
[35] V. Heinonen, C. V. Achim, K. R. Elder, S. Buyukdagli, and T. Ala-Nissila, Phys. Rev. E **89**, 032411 (2014).

[36] V. Heinonen, C. V. Achim, J. M. Kosterlitz, S.-C. Ying, J. Lowengrub, and T. Ala-Nissila, Phys. Rev. Lett. **116**, 024303 (2016).

[37] B. P. Athreya, N. Goldenfeld, J. A. Dantzig, M. Greenwood, and N. Provatas, Phys. Rev. E **76**, 056706 (2007).

[38] M. Greenwood, J. J. Hoyt, and N. Provatas, Acta Mater. **57**, 2613 (2009).

[39] M. Greenwood, Using phase-field modeling with adaptive mesh refinement to study elasto-plastic effects in phase transformations, Ph.D. thesis, McMaster University, 2008.